Comput. Methods Appl. Mech. Engrg. 200 (2011) 2859–2870

Contents lists available at ScienceDirect

Comput. Methods Appl. Mech. Engrg.

journal homepage: www.elsevier.com/locate/cma

A Nitsche-extended finite element method for earthquake rupture on complex fault systems

E.T. Coon [a,*], B.E. Shaw [b], M. Spiegelman [a,b]

[a] Applied Physics and Applied Mathematics, Columbia University, 200 S.W. Mudd Bldg, 500 W 120th St., New York, NY 10027, USA
[b] Lamont Doherty Earth Observatory, Columbia University, 61 Route 9w, Palisades, NY 10964, USA

ARTICLE INFO

Article history:
Received 14 June 2010
Received in revised form 12 May 2011
Accepted 16 May 2011
Available online 25 May 2011

Keywords:
XFEM
Nitsche's method
Earthquakes
Fault systems

ABSTRACT

The extended finite element method (XFEM) provides a natural way to incorporate strong and weak discontinuities into discretizations. It alleviates the need to mesh discontinuities, allowing simulation meshes to be nearly independent of discontinuity geometry. Currently, both quasistatic deformation and dynamic earthquake rupture simulations under standard FEM are limited to simplified fault networks, as generating meshes that both conform with the faults and have appropriate properties for accurate simulation is a difficult problem. In addition, fault geometry is not well known; robustness of solution to fault geometry must be determined. Remeshing with varying geometry would make such tests computationally unfeasible. The XFEM makes a natural choice for discretization in these crustal deformation simulations on complex fault systems. Here, we develop a method based upon the XFEM using Nitsche's method to apply boundary conditions, enabling the solution of static deformation and dynamic earthquake models. We compare several approaches to calculating and applying frictional tractions. Finally, we demonstrate the method with two problems: an earthquake community dynamic code verification benchmark and a quasistatic problem on a fault system model of southern California.

Published by Elsevier B.V.

1. Introduction

Modeling earthquakes and geologically short time-scale events on fault networks is a rich problem with important implications for human safety and engineering design. In order to quantitatively model earthquakes, scientists must incorporate an extremely complex network of intersecting faults. Incorporating this geometry accurately has proven crucial in the simulation of both earthquake rupture and long-term quasistatic deformation [3,8,30]. Computationally, this provides a stern challenge for modelers – static and dynamic equations must be solved on domains with many faults characterized by large variation in length, orientation, density, and connectivity.

Crustal deformation simulation is similar, but not identical, to engineering problems such as contact problems and crack growth problems. Unlike contact problems, lithostatic pressure ensures that faults are kept in contact, and strains are generally small, indicating that linear elasticity without cavitation is a good approximation. Unlike crack growth problems, earthquakes repeatedly rupture pre-existing weak faults, and the fault system is generally assumed to be fixed for any given simulation. However, mixed, history-dependent boundary conditions on these faults differ from typical contact and crack growth problems, and provide unique difficulties to spatial discretization. See Scholz [36] and references therein for a summary of these observations.

Several techniques have been used to simulate crustal deformation. Boundary Integral Methods have been used in dynamic simulations with complex geometry [27,9,26,42], but cannot simulate nonlinear bulk rheologies, which play an important role in off-fault deformation. Finite differences allow simulations of long, repeated rupture problems [37,39,38], but are limited in their ability to incorporate complex fault system geometry. Here we focus on Finite Element Methods (FEM), which have the ability to incorporate bulk rheology and nonplanar fault geometry [1,14].

In order to incorporate faults into the FEM, the computational mesh must align with faults and exhibit aspect ratios and other properties for accurate simulation. Some three-dimensional simulations of realistic fault structures have been done for limited regional models (for example, in quasistatic tectonic deformation simulations [29] and subsistence in geomechanical simulations [19]). However, generating appropriate three-dimensional meshes on domains such as the entirety of tectonically active faults near a plate boundary (such as the 243 faults identified in one Southern California model [43]) is a difficult problem. In addition, fault

* Corresponding author. Tel.: +1 917 969 6831.
E-mail address: ecoon@lanl.gov (E.T. Coon).

0045-7825/$ - see front matter Published by Elsevier B.V.
doi:10.1016/j.cma.2011.05.005

geometry is uncertain; under the FEM, to test the robustness of simulations to changes in fault geometry, the mesh must change.

As an alternative, mesh-independent finite element methods can capture discontinuous fields on fault geometries. In particular, the eXtended Finite Element Method (XFEM), as developed by Belytschko and colleagues [7,33,13] and modified by Fries [20], extends the finite function space to include both discontinuous functions across the fault and tip functions which match the stress singularity of elasticity at crack tips. This method, based upon the partition of unity FEM [31,15], allows faults to cut elements in a nearly-arbitrary way, making it an ideal choice for complicated fault geometries. It has been applied successfully to applications of crack growth [33], Stokes flow [44], biofilms [16], and other problems where material or physical interfaces play an important role. This, however, represents the first application to our knowledge to crustal deformation and earthquake dynamics.

Fault physics simulation is not, however, a trivial implementation of the XFEM. In these types of problems, boundary conditions along the faults are of mixed type depending on whether the fault is stuck or slipping, and additional interpenetration constraints are required. Most of the difficult physics in these models arise from friction and failure processes, so an accurate treatment of boundary conditions is required.

Typical finite element methods for earthquake rupture rely on interpolatory relations on the fault boundary to track failure. These methods keep stress at a set of mesh nodes: basis functions $\{\psi_i\}$ have a corresponding set of mesh nodes $\{\mathbf{x}_i\}$ such that

$$\psi_i(x_j) = \delta_{ij}, \tag{1}$$

at which essential boundary conditions can be evaluated and applied in a strong sense. These methods for rupture detection and propagation are often called Traction at Split Nodes (TaSN) in the crustal deformation literature, and have been used in both finite difference and finite element methods [2,11,1]. This is not possible in the XFEM, where mesh nodes do not lie on the boundary. We must use a weak formulation of boundary conditions and a corresponding weak formulation to track the rupture front along the fault. While a weak formulation of boundary conditions is computationally more complex than TaSN methods, it is also mathematically more general, and can be used for higher-order and spectral FEM.

The weak application of boundary conditions has been proposed in many ways. Lagrange multiplier methods [4] and penalty methods [5] are the most common approaches. Lagrange multiplier methods require the construction of a dual function space for tractions which satisfy the Ladyzhenskaya-Babuska-Brezzi (LBB) condition [4,10]. Ji and Dolbow [25] and Moes et al. [32] point out that the simplest approach of defining the dual space on the boundary via intersection of the crack with elements of the domain mesh does not satisfy this condition. Moes et al. [32] provides an algorithm for determining a subset of intersections to use as elements and calculates a mesh on the boundary that can be numerically tested for the LBB condition. However, this approach is extremely mesh dependent and is not obviously extensible to three dimensions. The most basic penalty methods typically result in ill-conditioned systems of equations.

Nitsche's method [35], as developed for this type of problem by Hansbo and Hansbo [21], provides another way to apply essential boundary conditions weakly through an alternate bilinear form. This method can be thought of as a hybrid of penalty methods and Lagrange multiplier methods, and results in a symmetric bilinear form. The resulting stabilized linear equations are better conditioned than standard penalty methods, and they avoid saddle-point problem complications inherent to Lagrange multiplier methods. Nitsche's method has been used in contact problems under standard finite element methods [45], and more recently in extended finite element methods [12], and are similar to other stabilized methods such as [34,28].

Once a solution for displacement is determined, tractions on the fault are calculated to determine the location of the rupture front. On regions where the fault is still stuck, a Dirichlet boundary condition is applied. The tractions necessary to keep that fault stuck are compared to a failure criteria. This type of calculation, by which a solution on the full domain must be used to determine the pointwise value of a function on the boundary, has been attempted in several ways. One such way is the use of Lagrange multipliers, which provides the traction as the solution of the dual variable. Ji and Dolbow [25] and Mourad et al. [34] propose a domain integral method, which uses the simple dual space on cracks with a local stabilization. The most basic application of this technique as in [25] results in a smoothed solution for tractions in contact problems. However, actual tractions in the earthquake problem can be discontinuous at the rupture front and at fault kinks and branches. Here we introduce an approach which uses a discontinuous dual function space to capture discontinuous tractions.

In this paper, we consider a Nitsche- extended finite element method for discretization of a model of crustal deformation. We use Nitsche's method to stabilize the problem, the XFEM to discretize the weak formulation, and a smoothed inversion for calculating tractions on the boundary. We compare this approach to a domain integral method for stabilized tractions. The resulting approach is more versatile than domain integral methods, as it can be designed to more accurately include geometric discontinuities in tractions along the fault. This enables tracking when a point on the fault ruptures or sticks, which requires a change in the type of boundary condition at that point. The resulting approach is natural for the mixed, history dependent boundary conditions inherent to crustal deformation.

We apply the method to problems of dynamic rupture and static relaxation on complex fault networks. Several major simplifications from the earth are made here. Most notably, we consider only two-dimensional problems as a prototype for future three-dimensional simulations. Indeed, two-dimensional fault models are trivially meshed via Delaunay triangulation, limiting the advantages of the XFEM. However, two-dimensional problems provide an excellent proof-of-concept for the method. XFEM has been used in three-dimensions for material failure [41,17], and Nitsche's method and traction determination are extended to three dimensions in a straightforward manner. Extension of the approaches here to three-dimensions are theoretically straightforward, but computationally complex. Therefore, two-dimensional prototypes for the method are an important step.

The equations of dynamic earthquake rupture are shown in Section 2, and a quasistatic simplification is discussed. In Section 3 the method is presented: Section 3.1 applies Nitsche's method to generate a symmetric, coercive weak formulation of the problem incorporating mixed stickslip boundary conditions. Section 3.2 discretizes the spatial component of equations for displacement via the XFEM. Section 3.3 presents a stabilized inversion to determine a solution for tractions on the faults, updating friction and testing the fault for regions which have failed or stuck. The method is demonstrated through a series of example problems in Section 4. This work represents an important connection between the newly developing numerical techniques of Nitsche-XFEM and crustal deformation models, which benefit greatly from computational advantages of the combined method.

2. Earthquake rupture physics

We wish to solve static and dynamic linear elasticity equations for displacement $\mathbf{u}$ on a domain $\Omega - \Gamma \subset R^2$, where Γ consists of a system of faults, $\Gamma \equiv \bigcup \Gamma^i$, which are lower-dimensional subspaces

of Ω. In-plane (Mode II) displacement $\mathbf{u}$ is governed by the solution of momentum balance, under isotropic linear elasticity:

$$\rho \frac{\partial^2 \mathbf{u}}{\partial t^2} = \nabla \cdot \boldsymbol{\sigma}(\mathbf{u}), \tag{2}$$

$$\boldsymbol{\sigma} \equiv \boldsymbol{\sigma}(\mathbf{u}) = \lambda \, \mathbf{tr}(\boldsymbol{\epsilon}(\mathbf{u}))\boldsymbol{I} + 2\mu\boldsymbol{\epsilon}(\mathbf{u}), \tag{3}$$

$$\boldsymbol{\epsilon} \equiv \boldsymbol{\epsilon}(\mathbf{u}) = \frac{1}{2}(\nabla \mathbf{u} + (\nabla \mathbf{u})^T), \tag{4}$$

where ρ is the density, $\boldsymbol{\sigma}$ stress, $\boldsymbol{\epsilon}$ strain, λ and μ are Lamé's parameters, and $\boldsymbol{I}$ is the identity tensor. Throughout, bold quantities represent vectors or tensors in R^2, while standard font indicates scalar quantities. This vector-valued equation is subjected to mixed boundary conditions. On the exterior boundary, $\partial\Omega$, displacement is specified as

$$\mathbf{u}|_{\partial\Omega} = \boldsymbol{v}_p T, \tag{5}$$

where v_p is a tectonic loading rate which is much smaller than the wave speed. This results in a separation of scales, where $T = t_0 + t$, for a long time-scale t_0 and a perturbation (dynamic) time t. In the loading, variations in t are ignored, and this boundary condition becomes a constant depending only on the long time-scale:

$$\mathbf{u}|_{\partial\Omega} = \boldsymbol{v}_p t_0. \tag{6}$$

Interior boundary conditions are specific to the two problems considered: static deformation and dynamic rupture. In the static case, derivatives with respect to time are eliminated, and interior boundary conditions are of the form:

$$[\![\mathbf{u}]\!]_{\Gamma^D} \cdot \hat{\mathbf{t}} = g, \tag{7}$$

$$\hat{\mathbf{t}} \cdot \langle \boldsymbol{\sigma} \rangle_{\Gamma^N} \cdot \hat{\mathbf{n}} = f, \tag{8}$$

$$[\![\mathbf{u}]\!]_{\Gamma} \cdot \hat{\mathbf{n}} = 0, \tag{9}$$

where $[\![\cdot]\!]_\Gamma$ and $\langle \cdot \rangle_\Gamma$ indicate the jump (difference) and mean value across Γ, respectively, $\hat{\cdot}$ indicates a unit vector, and $\hat{\mathbf{n}}$ and $\hat{\mathbf{t}}$ are oriented normal and tangential to Γ, respectively. Faults Γ are split into two sets: Γ^D, on which slip g is provided (essential boundary conditions), and Γ^N on which tractions f are provided (natural boundary conditions). On the entire fault system, neither dilation nor interpenetration is allowed. Throughout, we refer to Eqs. (2)–(9) as the static case.

In the case of dynamic rupture, boundary conditions are given by:

$$\left[\!\!\left[\frac{\partial \mathbf{u}}{\partial t}\right]\!\!\right]_{\Gamma^D} \cdot \hat{\mathbf{t}} = 0, \tag{10}$$

$$\hat{\mathbf{t}} \cdot \langle \boldsymbol{\sigma} \rangle_{\Gamma^N} \cdot \hat{\mathbf{n}} = f, \tag{11}$$

$$[\![\mathbf{u}]\!]_{\Gamma} \cdot \hat{\mathbf{n}} = 0. \tag{12}$$

Γ is again partitioned into two sets. On Γ^D, the stuck portions of Γ, a no slip condition is enforced. On Γ^N, the slipping portions of Γ, tractions f apply friction. Again, neither interpenetration nor cavitation is allowed.

In both problems, shear stress $\tau(\mathbf{u}) \equiv \hat{\mathbf{t}} \cdot \langle \boldsymbol{\sigma}(\mathbf{u}) \rangle_{\Gamma^N} \cdot \hat{\mathbf{n}}$ is balanced by friction $f = \Phi\sigma_n(\mathbf{u}) = \Phi(\hat{\mathbf{n}} \cdot \langle \boldsymbol{\sigma}(\mathbf{u}) \rangle_{\Gamma^N} \cdot \hat{\mathbf{n}})$, which is assumed a product of normal stress and a coefficient of friction. The coefficient of friction Φ is often a nonlinear function of slip, slip-rate, and other state variables, and includes a signed direction opposing slip rate.

The two sets Γ^D and Γ^N partition the faults Γ. Points on the faults transition between the two sets by a history-dependent criteria. A point x on Γ^D fails when shear stress exceeds a maximum frictional strength:

$$\forall \mathbf{x} \in \Gamma^D \quad \text{s.t.} \quad \frac{|\tau|}{\sigma_n} \geqslant |\Phi| \;\Rightarrow\; \mathbf{x} \in \Gamma^N \tag{13}$$

and sticks when slip rate returns to zero:

$$\forall \mathbf{x} \in \Gamma^N \quad \text{s.t.} \quad \left[\!\!\left[\frac{\partial \mathbf{u}}{\partial t}\right]\!\!\right]_{\mathbf{x}} = 0 \;\Rightarrow\; \mathbf{x} \in \Gamma^D. \tag{14}$$

Note that in these problems, we restrict consideration to the compressional situations appropriate for the earth, where $\sigma_n > 0$. The dynamic problem therefore consists of Eqs. (2)–(5), (6), (11)–(14).

Loosely, the full earthquake cycle consists of alternating periods of interseismic loading via slow, static deformation over periods of hundreds to hundreds of thousands of years, and earthquakes, which are dynamic ruptures over periods of one to hundreds of seconds. For this paper, we consider the two independently in this simplified form. Future work combines the two, modeling the full repeated earthquake rupture cycle.

3. Numerical technique

The solution of these equations must be accomplished on general fault system domains, where fault geometry Γ can often be an extremely complicated set of intersecting subdomains. The finite element method provides a natural selection to discretize these equations, as its local function spaces can be designed to accommodate fault geometry. The weak form of the equilibrium equations under the Galerkin method is to find $\mathbf{u} \in \mathcal{V}$ so that

$$\forall \mathbf{v} \in \mathcal{V}, \int_\Omega \boldsymbol{\epsilon}(\mathbf{v}) : \boldsymbol{\sigma}(\mathbf{u}) = \int_{\Gamma^N} ([\![\mathbf{v}]\!]_\Gamma \cdot \hat{\mathbf{t}}) f + \int_{\Gamma^D} \mathbf{v} \cdot \boldsymbol{\sigma}(\mathbf{u}) \cdot \hat{\mathbf{n}} + \int_{\Gamma^N} ([\![\mathbf{v}]\!] \cdot \hat{\mathbf{n}})(\hat{\mathbf{n}} \cdot \boldsymbol{\sigma}(\mathbf{u}) \cdot \hat{\mathbf{n}}). \tag{15}$$

Natural boundary conditions f are included, but terms for the normal component of slip and the essential boundary conditions have not yet been included. Under the FEM, admissible functions for $\mathbf{u}$ are limited to come from a function space $\mathcal{V}_g$ which is a subset of $\mathcal{H}^1_g$, Hilbert spaces of the needed regularity that match Dirichlet boundary data g on Γ^D and have zero normal component on Γ^N, while test functions $\mathbf{v}$ are taken from $\mathcal{H}^1_0$, which are 0 on all Dirichlet boundaries. Matching $\mathbf{u}$ on the Dirichlet boundary is equivalent to constructing $\mathcal{V}_g \subset \mathcal{H}^1_g$. Such a construction is difficult if not impossible in the XFEM with mixed boundary conditions.

Therefore, we use a weak formulation for including essential conditions on the fault.

3.1. Nitsche's method

Nitsche's method considers an alternate formulation of the weak form for Galerkin finite element methods. An in-depth derivation of the resulting bilinear forms is demonstrated in the Appendix A. Applied to the static problem, we look to find a solution $\mathbf{u}$ to:

$$\mathcal{B}(\mathbf{u}, \mathbf{v}) = \ell(\mathbf{v}) \quad \forall \quad \mathbf{v} \in \mathcal{V}, \tag{16}$$

where

$$\begin{aligned}
\mathcal{B}(\mathbf{u}, \mathbf{v}) = & \int_\Omega \boldsymbol{\epsilon}(\mathbf{v}) : \boldsymbol{\sigma}(\mathbf{u}) \qquad (*) \\
& - \int_\Gamma ([\![\mathbf{v}]\!]_\Gamma \cdot \hat{\mathbf{n}})\sigma_n(\mathbf{u}) + \sigma_n(\mathbf{v})([\![\mathbf{u}]\!]_\Gamma \cdot \hat{\mathbf{n}}) \qquad (a1) \\
& + \frac{\beta_l}{h} \int_\Gamma ([\![\mathbf{v}]\!]_\Gamma \cdot \hat{\mathbf{n}})([\![\mathbf{u}]\!]_\Gamma \cdot \hat{\mathbf{n}}) \qquad (a2) \\
& - \int_{\Gamma^D} ([\![\mathbf{v}]\!]_{\Gamma^D} \cdot \hat{\mathbf{t}}|)\tau(\mathbf{u}) + \tau(\mathbf{v})|([\![\mathbf{u}]\!]_{\Gamma^D} \cdot \hat{\mathbf{t}}) \qquad (b1) \\
& + \frac{\beta_D}{h} \int_{\Gamma^D} ([\![\mathbf{v}]\!]_{\Gamma^D} \cdot \hat{\mathbf{t}}|)|([\![\mathbf{u}]\!]_{\Gamma^D} \cdot \hat{\mathbf{t}}) \qquad (b2) \\
& - \int_{\partial\Omega} \mathbf{v} \cdot \boldsymbol{\sigma}(\mathbf{u}) \cdot \hat{\mathbf{n}} + \boldsymbol{\sigma}(\mathbf{v}) \cdot \hat{\mathbf{n}} \cdot \mathbf{u} \qquad (c1) \\
& + \frac{\beta_{\partial\Omega}}{h} \int_{\partial\Omega} \mathbf{v} \cdot \mathbf{u} + (\mathbf{v} \cdot \hat{\mathbf{n}})(\mathbf{u} \cdot \hat{\mathbf{n}}) \qquad (c2)
\end{aligned} \tag{17}$$

$$\begin{aligned}\ell(\mathbf{v}) = &\int_{\Gamma^N}([\![\mathbf{v}]\!]_{\Gamma^N}\cdot\hat{\mathbf{t}})f \qquad (*)\\ &-\int_{\Gamma^D}\tau(v)g \qquad (b1)\\ &+\frac{\beta_D}{h}\int_{\Gamma^D}([\![\mathbf{v}]\!]_{\Gamma^D}\cdot\hat{\mathbf{t}})g \qquad (b2)\\ &-\int_{\partial\Omega}\boldsymbol{\sigma}(\mathbf{v})\cdot\hat{\mathbf{n}}\cdot\boldsymbol{v}_p t \qquad (c1)\\ &+\frac{\beta_{\partial\Omega}}{h}\int_{\partial\Omega}\mathbf{v}\cdot\boldsymbol{v}_p t+(\mathbf{v}\cdot\hat{\mathbf{n}})(\boldsymbol{v}_p t\cdot\hat{\mathbf{n}}) \qquad (c2).\end{aligned} \tag{18}$$

The $(*)$ terms are the typical FEM weak formulation, where the divergence of $\boldsymbol{\sigma}$ has been moved to the test function $\mathbf{v}$, and natural boundary terms from (8) arise in the linear form. Each lettered couple applies a separate essential boundary condition. In each couple, the (1) term is similar to the terms in standard FEM which are eliminated by assuming $\mathbf{v}|_{\Gamma^D}=0$, while the (2) term penalizes a mismatch with the boundary condition. Term (a) applies the no interpenetration constraint (9) with constant penalty coefficient β_I, (b) applies essential boundary conditions (7) with penalty coefficient β_D, and (c) applies Dirichlet boundary data (6) on the exterior boundary with penalty coefficient $\beta_{\partial\Omega}$. h is a measure of the element size.

Similarly, for the dynamic case,

$$\begin{aligned}\mathcal{B}(\mathbf{u},\mathbf{v}) = &\int_\Omega \rho\mathbf{v}\cdot\frac{\partial^2\mathbf{u}}{\partial t^2}+\int_\Omega \boldsymbol{\epsilon}(\mathbf{v}):\boldsymbol{\sigma}(\mathbf{u}) \qquad (*)\\ &-\int_\Gamma([\![\mathbf{v}]\!]_\Gamma\cdot\hat{\mathbf{n}})\sigma_n(\mathbf{u})+\sigma_n(\mathbf{v})([\![\mathbf{u}]\!]_\Gamma\cdot\hat{\mathbf{n}}) \qquad (a1)\\ &+\frac{\beta_I}{h}\int_\Gamma([\![\mathbf{v}]\!]_\Gamma\cdot\hat{\mathbf{n}})([\![\mathbf{u}]\!]_\Gamma\cdot\hat{\mathbf{n}}) \qquad (a2)\\ &-\int_{\Gamma^D}([\![\mathbf{v}]\!]_{\Gamma^D}\cdot\hat{\mathbf{t}}|)\tau(\mathbf{u})+\tau(\mathbf{v})|([\![\mathbf{u}]\!]_{\Gamma^D}\cdot\hat{\mathbf{t}}) \qquad (b1)\\ &+\frac{\beta_D}{h}\int_{\Gamma^D}([\![\mathbf{v}]\!]_{\Gamma^D}\cdot\hat{\mathbf{t}}|)|\left([\![\frac{\partial\mathbf{u}}{\partial t}]\!]_{\Gamma^D}\cdot\hat{\mathbf{t}}\right) \qquad (b2)\\ &-\int_{\partial\Omega}\mathbf{v}\cdot\boldsymbol{\sigma}(\mathbf{u})\cdot\hat{\mathbf{n}}+\boldsymbol{\sigma}(\mathbf{v})\cdot\hat{\mathbf{n}}\cdot\mathbf{u} \qquad (c1)\\ &+\frac{\beta_{\partial\Omega}}{h}\int_{\partial\Omega}\mathbf{v}\cdot\mathbf{u}+(\mathbf{v}\cdot\hat{\mathbf{n}})(\mathbf{u}\cdot\hat{\mathbf{n}}) \qquad (c2)\end{aligned} \tag{19}$$

$$\begin{aligned}\ell(\mathbf{v}) = &\int_{\Gamma^N}([\![\mathbf{v}]\!]_{\Gamma^N}\cdot\hat{\mathbf{t}})f \qquad (*)\\ &-\int_{\partial\Omega}\boldsymbol{\sigma}(\mathbf{v})\cdot\hat{\mathbf{n}}\cdot\boldsymbol{v}_p t \qquad (c1)\\ &+\frac{\beta_{\partial\Omega}}{h}\int_{\partial\Omega}\mathbf{v}\cdot\boldsymbol{v}_p t+(\mathbf{v}\cdot\hat{\mathbf{n}})(\boldsymbol{v}_p t\cdot\hat{\mathbf{n}}) \qquad (c2).\end{aligned} \tag{20}$$

Again, the $(*)$ terms are the typical FEM weak formulation, (a) applies the no interpenetration constraint (12), (b) applies no slip conditions (10) on stuck boundaries, and (c) applies Dirichlet boundary data (6) on the exterior boundary. Note that frictional terms, despite being nonlinearly dependent upon $\mathbf{u}$, are included in the linear form. These terms are incorporated via lagging or fixed-point iteration.

These bilinear forms are derived from a minimization problem discussed in the Appendix A, and apply both Neumann and Dirichlet boundary data weakly. Note that, assuming boundary conditions are satisfied, all (2) terms and the second part of all (1) terms cancel, and the method is consistent with the usual weak formulation. Given the symmetry of the stiffness term in (19)*, $\mathcal{B}$ is symmetric. For large enough β's, $\mathcal{B}$ is also coercive, as demonstrated in a similar example by Heintz and Hansbo [24]. They also demonstrate a sufficient condition on the penalty terms for coercivity, which guide the selection of the constants β. Noting that a coercive bilinear form indicates that the residual grows more rapidly than the error, combined coercivity and symmetry indicate that the resulting linear system is easily solved by many methods, and simpler to solve than most saddle-point, Lagrange multiplier systems. Therefore the choice of β is a careful balance. It should be chosen large enough to result in a coercive operator, and the larger the β, the less mismatch at the boundary. However, if β is chosen to be too large, the problem becomes unnecessarily expensive (as the operator is ill-conditioned). This choice can be made independently of mesh resolution (as h-dependence is included explicitly in the above equations). Therefore the choice should be made to balance a desire for accuracy and performance. Here we simply choose β to be large, as performance is not as much of an issue.

3.2. XFEM

As with other Galerkin FEMs, the test functions $\mathbf{v}$ and solution $\mathbf{u}^h$ are chosen from the same discrete function space, $\mathcal{V}^h\subset\mathcal{V}$. This space is continuous on the domain, but must allow discontinuities across faults Γ. The eXtended Finite Element Method (XFEM) provides a natural setting for encoding both strong and weak discontinuities into the function space.

First, Ω is meshed with nodes $\{x_i\}$ independently of the faults. A partition of unity function space is specified on this mesh; we use a regular quadrilateral mesh with bilinear "hat" basis functions $\widehat{\psi_i}$ which are 1 at x_i and 0 at all other nodes. Around each node x_i, a local neighborhood, Ω^i, is defined to be the support of $\widehat{\psi_i}$ (in this case the four quadrilaterals bordering x_i). Then this space is extended with additional basis functions consisting of products of the bilinear functions and extension functions. These extension functions are chosen to accurately capture the physics across cracks, at crack tips, and at crack junctions. For a more explicit derivation, see Dolbow et al. [13] and Fries [20]; here we simply state the resulting discrete approximation space. The final function space is the span of the bilinear basis functions and the extended basis functions:

$$\mathcal{V}^h\equiv\operatorname{span}\left(\{\widehat{\psi_i}\},\bigcup_{I^j}\{H^j(x)\widehat{\psi_i}\}_{i\in P^j},\bigcup_{x^{jk}_{branch}}\{H^{jk}(x)\widehat{\psi_i}\}_{i\in Q^j},\bigcup_{x^j_{tip}}\{F^j(x)\widehat{\psi_i}\}_{i\in R^j}\right), \tag{21}$$

where the following definitions have been made:

- Define Γ to be a union of curves, $\bigcup_j \Gamma^j$.
- If Γ^j branches from Γ^k, call the branching point x^{jk}_{branch}.
- Otherwise, let x^j_{tip} be the location of the tip.
- *Crack Extensions:* Nodes x_i whose neighborhood Ω^i is bisected by Γ^j are extended with sign functions defined on a local coordinate system based upon Fig. 1:

$$H^j(x)\equiv\begin{cases}1 & \text{if } (x-y)\cdot\hat{\mathbf{n}}(y)>0,\\ -1 & \text{otherwise},\end{cases} \tag{22}$$

$$\text{where } y\equiv\arg\min_{z\in\Gamma}|x-z|$$

$$P^j\equiv\{i \quad \text{s.t.} \quad \Omega^i\cup\Gamma^j\neq 0, i\notin Q^j,R^j\}. \tag{23}$$

- *Branch Extensions:* Nodes x_i whose neighborhood Ω^i contain a branch point are extended with a junction sign function. This is effectively a sign function defined with the jump across both the branching crack and all of the branched crack on one side of the branch point. Typically a crack extension associated with crack Γ^k and a junction function associated with crack Γ^j are added, so that there are three degrees of freedom – unity, sign extensions across crack k, and sign extensions across crack j and part of crack k. This treats the junction like a triple point:

$$H^{jk}(x)\equiv\begin{cases}H^j(x) & \text{if } H^k(\Gamma^j)=H^k(x),\\ H^k(x) & \text{otherwise},\end{cases} \tag{24}$$

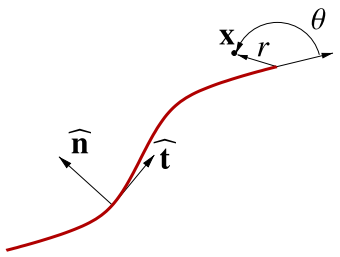

Fig. 1. Coordinate system used in defining extension functions near the fault system. Faults are defined with an arbitrary direction which defines $\hat{\mathbf{t}}$. The normal is then chosen via a right-hand rule, and Heaviside functions defined by this normal. Each tip has its own local polar coordinate system to define the tip function.

$$Q^j \equiv \left\{ i \quad \text{s.t.} \quad x^{jk}_{branch} \in \Omega^i \right\}. \tag{25}$$

- *Tip Extensions:* Tip extension functions are defined in a polar coordinate system around the tip, where the branch cut is at the crack (Fig. 1). The extension is chosen to match the singularity associated with linear elastic crack tips. Blending elements (as defined by Fries [20]) are added to smoothly transition from crack extensions to tip extensions. These extensions are added to all local spaces whose nodes within a fixed radius R_{tol} of the tip. This radius stays fixed to ensure proper convergence rates.

$$F^j(x) \equiv \sqrt{r}\sin\left(\frac{\theta}{2}\right)\sum_{k\in\widehat{R^j}}\widehat{\psi_k}, \tag{26}$$

$$r \equiv \left|x - x^j_{tip}\right|,$$

$$\theta \quad \text{is the angle from the tangent of } \Gamma^j \text{ at } x^j_{tip} \text{ to } x - x^j_{tip},$$

$$\widehat{R^j} \equiv \left\{ k \quad \text{s.t.} \quad \left|x^k - x^j_{tip}\right| < R_{tol} \right\},$$

$$R^j \equiv \widehat{R^j} \cup \{\text{neighbors of } x^k \quad \text{for } k \in \widehat{R^j}\}. \tag{27}$$

Fig. 2 diagrams the sets of nodes P, Q, and R which are extended. These scalar functions are multiplied by canonical vectors to span the two-dimensional vector space under consideration.

3.3. Traction determination

Given a solution for displacement determined via Eq. (16) with basis functions from Eq. (21), tractions are calculated for use in friction and failure conditions. We must determine tractions which would have resulted in the same displacement solved using the mixed boundary conditions (10)–(12). In an all-Neumann problem with data $\mathbf{T}$, (16) results in

$$\mathbb{f} \equiv \int_\Gamma [\![\mathbf{v}]\!]_\Gamma \cdot \mathbf{T} = \int_\Omega \rho \mathbf{v} \cdot \frac{\partial^2 \mathbf{u}}{\partial t^2} + \int_\Omega \boldsymbol{\epsilon}(\mathbf{v}) : \boldsymbol{\sigma}(\mathbf{u}). \tag{28}$$

This linear form must be inverted for $\mathbf{T}$ pointwise on Γ. To do this, Γ is meshed to form elements Γ_e by introducing nodes $\mathbf{y}_k$ at intersections of Γ with edges of the mesh for Ω (and kinks, branches, and other physically relevant geometric complexity of the Γ^i), as in Fig. 3. On these elements, a function space is defined so that $\mathbf{T} = \sum_i T_i \phi_i$, where T_i are weights and ϕ_i are basis functions. Note that $\mathbf{T}$ need only be square-integrable, and physically should be discontinuous at fault kinks and at the rupture front. Discontinuous elements have the advantage of admitting tractions which are discontinuous at these geometric locations. Then,

$$\left(\int_\Gamma [\![\psi_i]\!]_\Gamma \cdot \phi_j\right)\mathbf{T}_j = \mathbb{f}. \tag{29}$$

Defining $\mathbb{P} = \int_\Gamma [\![\psi_i]\!]_\Gamma \cdot \phi_j$, we can solve the normal equations $\mathbb{P}^T\mathbb{P}T_j = \mathbb{P}^T\mathbb{f}$. This is poorly constrained due to our choice of fault meshes not satisfying the LBB condition, and has spurious oscillations. To deal with these, we introduce a smoothing term. Furthermore, we can take advantage of the fact that part of the solution is known, and introduce a term penalizing mismatches.

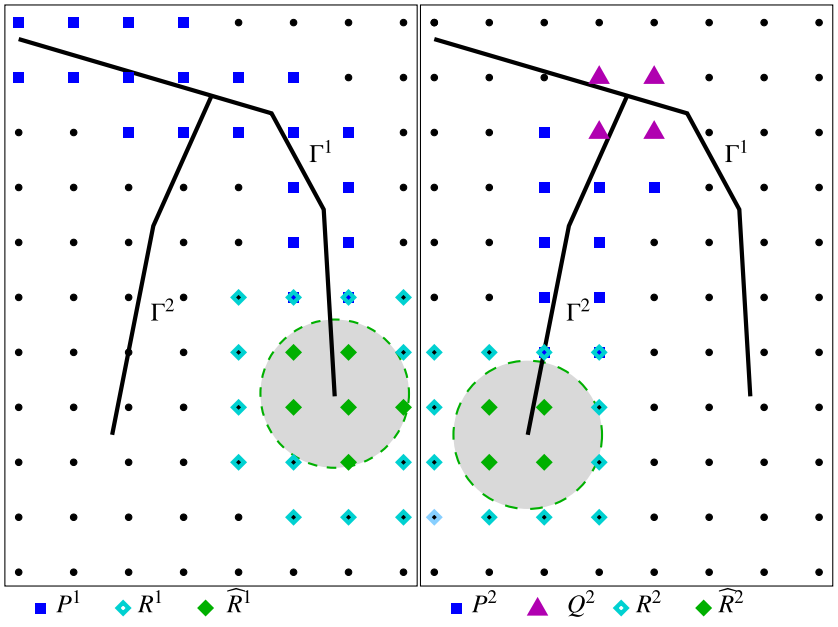

(a) Extensions on crack 1. (b) Extensions on crack 2.

Fig. 2. Sets of extended nodes for a crack system with two cracks, including one branching crack. Nodes are characterized by the intersection of their support (the neighboring four quadrilaterals) with the cracks Γ. Nodes labeled P are extended with Heaviside functions across the crack, as their support is cut completely by the fault. Nodes labeled Q are extended with branch functions, as their support contains the tip branching from another fault. Finally, nodes labeled R are extended with tip functions. $\bar{R}$ provides the support for these tip functions, blending the function into the background basis functions. All nodes, including those not extended, also hold the standard background finite element function, a bilinear hat function in this case.

$$\left(\mathbb{P}^T\mathbb{P} + \beta_d \int_\Gamma \frac{d\phi_i}{ds}\cdot\frac{d\phi_j}{ds} + \beta_m \sum_{\mathbf{y}_k\in S} |\phi_i\cdot\phi_j|\right)\mathbf{T}_j + \beta_N \int_{\Gamma^N} \phi_i\cdot\phi_j = \mathbb{P}^T\mathbb{f} + \beta_N \int_{\Gamma^N} \phi_i\tau. \quad (30)$$

Here, a penalty term β_d has been added to smooth the solution, where $\frac{d}{ds}$ indicates derivatives along the element curve. β_m enforces continuity of the discontinuous functions on element boundaries in the set S, which denotes nodes not at fault kinks. Finally, β_N utilizes the known portion of the tractions: the shear tractions on faults which are actively slipping.

This bilinear form is now inverted for weights $\mathbf{T}_i$, and normal and shear tractions are calculated via $\sigma_n = \hat{\mathbf{n}}\cdot\mathbf{T}$ and $\tau = \hat{\mathbf{t}}\cdot\mathbf{T}$.

Then, failure is handled on an element-by-element basis. Each element Γ_e fails according to the mean value of (13):

$$\forall \Gamma_e \in \Gamma^D \quad \text{s.t.} \quad \left|\int_{\Gamma_e} \mathbf{T}\cdot\hat{\mathbf{t}}\right| \geqslant \left|\int_{\Gamma_e} \Phi(\mathbf{T}\cdot\hat{\mathbf{n}})\right| \Rightarrow \Gamma_e \in \Gamma^N. \quad (31)$$

Similarly, re-sticking is checked on these elements according to the mean value of (14):

$$\forall \Gamma_e \in \Gamma^N \quad \text{s.t.} \quad \int_{\Gamma_e} [\![\frac{\partial \mathbf{u}}{\partial t}]\!]_{\Gamma_e}\cdot\mathbf{T} \leqslant 0 \Rightarrow \Gamma_e \in \Gamma^D. \quad (32)$$

3.4. Temporal discretization

In dynamic problems, it remains to finish discretizing the bilinear form (16) by introducing a timestepping scheme. Typically, timestepping in earthquake rupture simulation is done explicitly. By lumping mass matrices and lagging frictional terms, each timestep is accomplished in a single matrix multiply, allowing many events to be simulated with few computational resources. This comes at the expense of introducing dispersion and concerns about stiffness and stability.

With the XFEM, deriving lumped diagonal and block-diagonal mass matrices are a problem of active research [18]. As we are focused on the spatial discretization in this paper, here we use a standard semi-implicit, Crank-Nicolson timestepping scheme for temporal discretization.

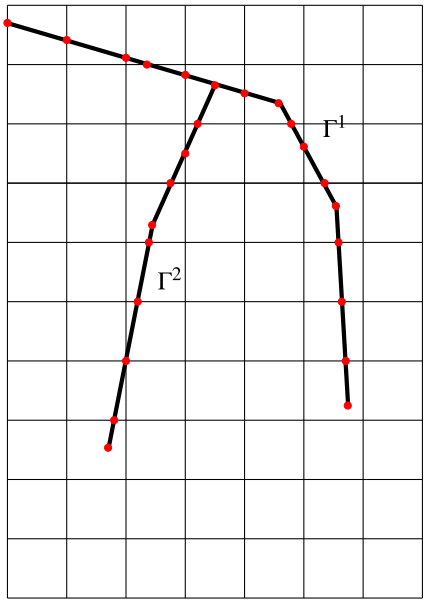

Fig. 3. Elements along the faults are defined by a mesh of nodes on the fault, which consists of the intersection of the faults with element edges of the background mesh, along with physically important nodes such as kinks and branches.

4. Examples

To test and demonstrate the method, we consider two simplified problems. All relevant parameters, both physical and

Table 1
Relevant parameters.

Variable	Value	Description
ρ	2670 kg/m^3	Density
$\lambda = \mu$	32.04 GPa	Lamé's parameters
$\boldsymbol{v}_p t_0$*	$\frac{70L}{\lambda}$ km	Boundary loading, background shear stress = 70 MPa
$\boldsymbol{v}_p t_0$†	$\frac{120L}{\lambda}$ km	Boundary loading, static problem
β_D, $\beta_{\partial\Omega}$	10^6	Penalty terms for stuck region, exterior boundary conditions
β_I^*	10^6	Penalty term for interpenetration
$\beta_I^\dagger$	10^2	Penalty term for interpenetration
β_d, β_m	10^{-2}	Smoothing and matching constraints
β_N	10^2	Penalty term to enforce known Neumann data
Φ_s, Φ_d^*	0.677, 0.525	Static and dynamic coefficients of friction
D_c^*	0.4 m	Critical slip length in friction
$\Phi_s^\dagger$	0.7	Static coefficient of friction

† Variables denote values specific to Example 4.2.
* Variables denote values specific to Example 4.1.

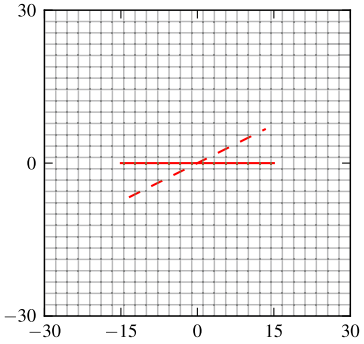

(a) Simulation domain, in kilometers. The grid shown is coarser by a factor of three than the coarsest mesh used in convergence tests.

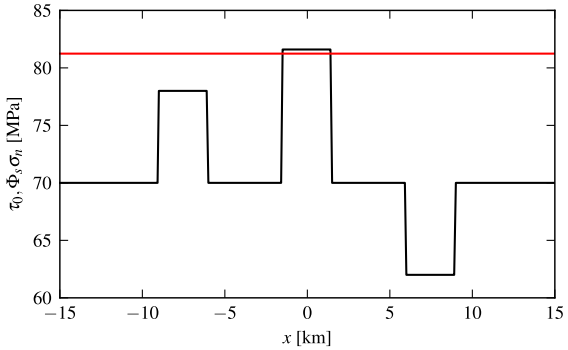

(b) Initial shear tractions and failure criteria.

Fig. 4. Domains for the unrotated (solid) and rotated (dashed) simulations. In the rotated case, exterior boundary conditions are adjusted to result in equivalent problems (in fault coordinates) to test mesh independence. Initial shear tractions (in black) specify strong ($\tau_0 = 62$ MPa), nucleation ($\tau_0 = 81.6$ MPa) and weak ($\tau_0 = 78$ MPa) patches along the fault. The nucleation patch is above the failure criteria, shown in red.

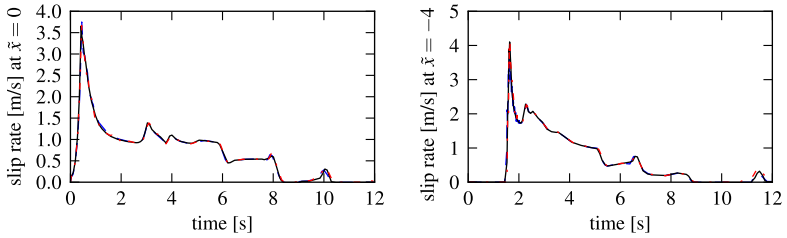

(a) Slip rate at the center of the nucleation patch.

(b) Slip rate outside of the nucleation patch.

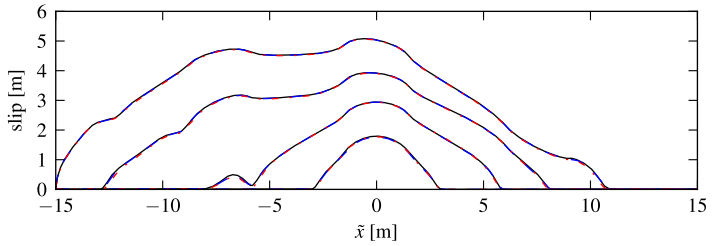

(c) Slip at 1, 2, 3, and 4 seconds after nucleation as the crack-like rupture propagates along the fault.

Fig. 5. Solutions of the SCEC Validation Exercise, Problem 205-2d. Black indicates the "true" solution, as calculated via a well-resolved solve (h = 25 m). Blue indicates an unrotated XFEM solution, where the fault lies on element boundaries. Red indicates a solution where the fault is rotated 30° relative to $y = 0$, where the fault is no longer coincident with the background mesh. In both simulations, the background mesh is a regular Cartesian grid (h = 100 m). Slip and slip rate are plotted in a fault-parallel coordinate system so that solutions should be identical. Despite the complexity of the solution, differences are not visible to the eye, demonstrating that the solution is qualitatively independent of mesh-fault orientation. Convergence rates for the rotated and unrotated fault are shown in Fig. 6(a). (For interpretation of the references to colour in this figure legend, the reader is referred to the web version of this article.)

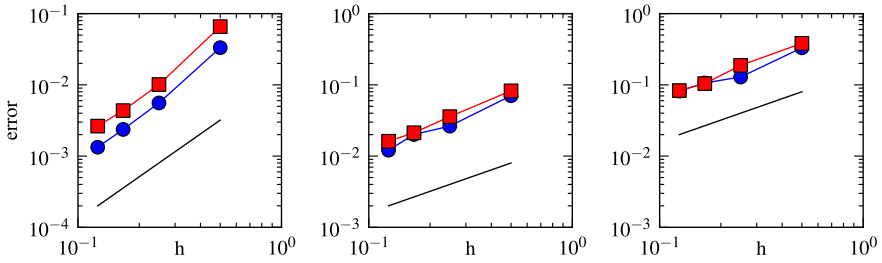

(a) Convergence rates of the L_2 error of slip.

(b) Convergence rates of the L_2 error of slip rate.

(c) Convergence rates of the L_2 error of tractions.

Fig. 6. Convergence rates of solutions solving the stabilized normal equations to invert for tractions in continuous piecewise linear elements. Blue circles indicate the unrotated case, red squares the rotated case. As expected, second order accuracy for slip and first order accuracy for the higher derivatives is seen in both the rotated and unrotated cases. (For interpretation of the references to colour in this figure legend, the reader is referred to the web version of this article.)

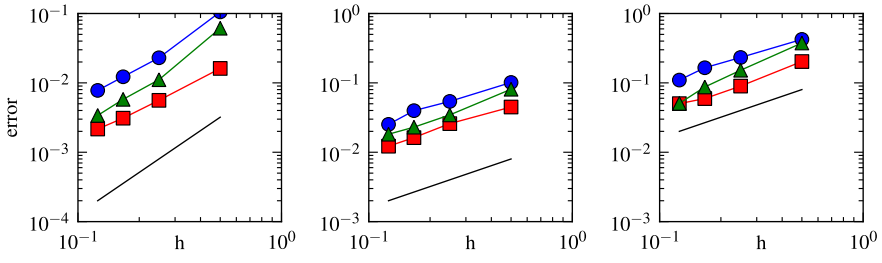

(a) Convergence rates of the L_2 error of slip.

(b) Convergence rates of the L_2 error of slip rate.

(c) Convergence rates of the L_2 error of tractions.

Fig. 7. Comparison of error using several techniques for inverting for tractions on the fault. Green (triangle glyphs) lines represent the domain integral method of [25], blue (circle) lines are the solutions of normal equations to invert for tractions using a continuous, piecewise linear function space, and red (square) lines use a discontinuous piecewise linear function space as proposed in Section 3.3. (For interpretation of the references to colour in this figure legend, the reader is referred to the web version of this article.)

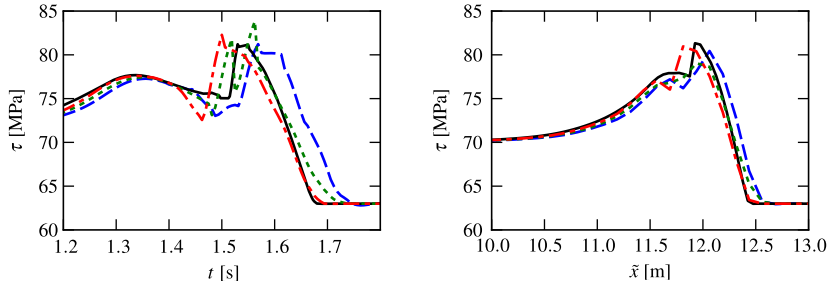

(a) Traction solution in time near the rupture front.

(b) Traction solution in space near the rupture front.

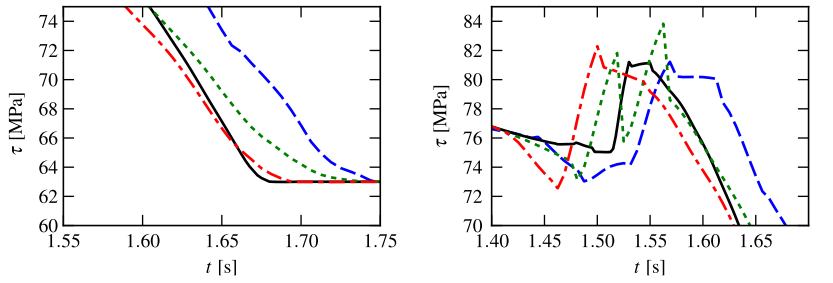

(c) Zoomed in around the rupture front.

(d) Zoomed in around the rupture peak.

Fig. 8. Error in the traction solution methods in time (a) and space (b). Black indicates the converged solution. Green, dotted lines are the domain integral method, blue, dashed lines are the continuous function space, and red, dash-dotted lines are the discontinuous function space. Zooming in around the rupture front (c) indicates that only the discontinuous method captures the arrival time correctly, while zooming in around the rupture peak (d) shows oscillations after the rupture, which are decreased in the discontinuous method. (For interpretation of the references to colour in this figure legend, the reader is referred to the web version of this article.)

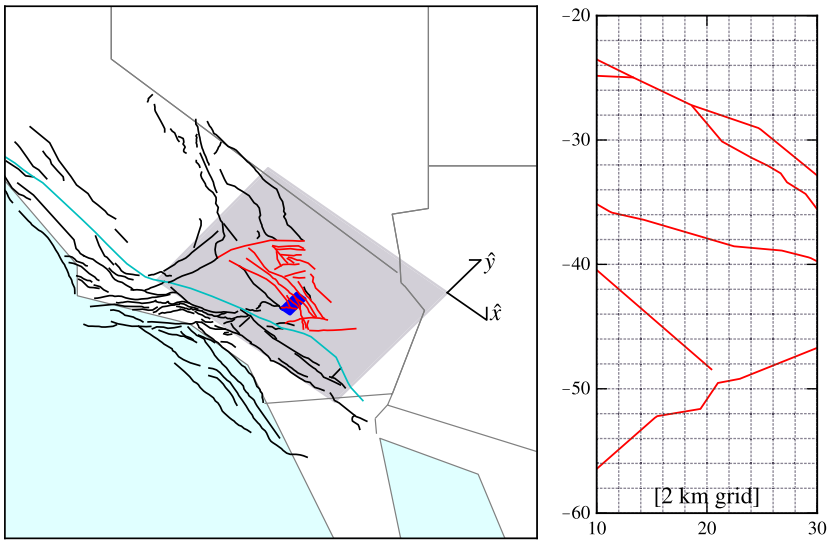

Fig. 9. Region of interest for the static example. All faults in the SCEC Community Fault Model Surface Traces are shown. The San Andreas fault is in blue, while faults included in the simulation are shown in red. The domain of simulation, on which a regular Cartesian background mesh is used, is the gray box. The domain is oriented parallel to plate motion, so that $\boldsymbol{v}_p = \boldsymbol{v}_p(y)$. A blowup (located at the blue box) is shown at right to demonstrate the actual simulation mesh, as compared to the faults. (For interpretation of the references to colour in this figure legend, the reader is referred to the web version of this article.)

mathematical, are shown in Table 1. Variables denoted with a * are specific to Example 4.1, and those denoted with a † are specific to Example 4.2.

4.1. Dynamic rupture benchmark

In the first example, we consider a single dynamic rupture in Mode II on a planar fault from the SCEC/USGS Earthquake Code Verification Exercise, Problem v. 205-2D [23]. These simulations solve Eqs. (16) and (19), (20), which include the inertial term and therefore radiated seismic waves. The domain is chosen to be the interval $[-L,L] \times [-L,L]$ ($L = 30$ km) with a single fault given by a 30 km segment centered at $(0,0)$ along the curve $y = 0$. Initial conditions are given by the solution to a static problem. This initial solve uses a specified shear traction which is uniformly at $\tau_U = 70$ MPa along the fault, with the exception of three patches: a "nucleation" patch at the center which is above failure, a "weak" patch, and a "strong" patch. Fig. 4 shows the simulation domain

and conditions on the fault. Exterior domain boundary conditions used to solve this initial condition are under the same uniform traction conditions.

At $t > 0$, the nucleation patch begins to weaken and slip. Friction is given by a slip-weakening law:

$$\Phi(\llbracket \mathbf{u} \rrbracket_{\Gamma^N}) = \Phi_s - \frac{(\Phi_s - \Phi_d)}{D_c} \left| \llbracket \mathbf{u} \rrbracket_{\Gamma^N} \right|. \tag{33}$$

In this frictional model, the coefficient of friction changes from a static value of Φ_s to a dynamic value of Φ_d over a critical slip length D_C. As the patch slips, stress near the patch increases, and a rupture begins to propagate along the fault with crack-like behavior. During the dynamic solve, exterior boundary conditions on $\partial\Omega$ are taken to be lowest-order radiating boundary conditions relative to the uniform stress solution, where

$$\frac{\partial \mathbf{u}}{\partial t} - (\boldsymbol{\sigma}(\mathbf{u}) \cdot \hat{\mathbf{n}} - \tau_U \hat{\mathbf{t}}) = 0 \tag{34}$$

to limit reflections from the exterior boundary as waves propagate from the rupturing fault.

To test the mesh independence of the method, we rotate the fault and conditions to a new coordinate system, $(\bar{x}, \bar{y})$, given by rotating θ degrees around (0,0), while keeping the background simulation mesh as a regular Cartesian mesh in (x,y). The solution in the rotated coordinate system is independent of θ, allowing the testing of the fault mesh independence of the simulation mesh. Solutions are summarized in Fig. 5, where tractions have been inverted to a continuous, piecewise linear finite element space, and convergence rates are shown in Fig. 6. Note that convergence is calculated by measuring the error at points corresponding to the nodes of the fault mesh on the coarsest simulation. Error is measured relative to a highly-resolved simulation, and L_2 norms of this error are shown. As expected, convergence of slip is nearly second order, with derivatives being first order. Note that the Crank-Nicolson time-stepping scheme used introduces dispersive error at the patch edges, which are discontinuous in traction. Error at later times in the dynamic simulation consists largely of a shift in the location of the rupture front.

Additionally, we compare three techniques for determining tractions on the fault: our penalized inversion where tractions

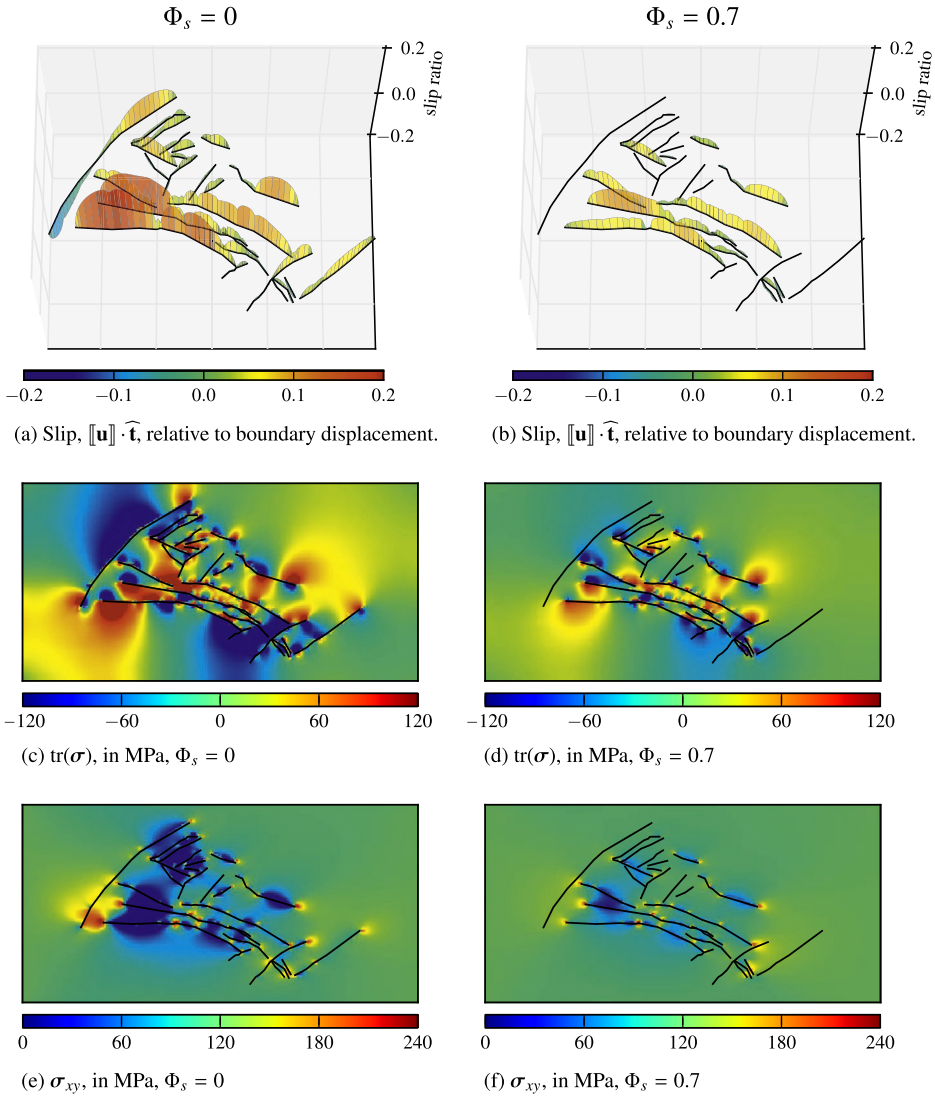

(a) Slip, $[\![\mathbf{u}]\!] \cdot \hat{\mathbf{t}}$, relative to boundary displacement.

(b) Slip, $[\![\mathbf{u}]\!] \cdot \hat{\mathbf{t}}$, relative to boundary displacement.

(c) tr($\boldsymbol{\sigma}$), in MPa, $\Phi_s = 0$

(d) tr($\boldsymbol{\sigma}$), in MPa, $\Phi_s = 0.7$

(e) $\boldsymbol{\sigma}_{xy}$, in MPa, $\Phi_s = 0$

(f) $\boldsymbol{\sigma}_{xy}$, in MPa, $\Phi_s = 0.7$

Fig. 10. Comparison of static simulations with zero friction and a constant frictional coefficient on a portion of the SCEC CFM in Southern California. In (a) and (b), nondimensional slip relative to the background loading displacement is shown as both height and color. Positive values represent right-lateral slip; negative values are left-lateral slip. With nonzero frictional coefficient, faults which are unfavorably oriented do not slip. Here, $\beta_{\partial\Omega} = \beta_D = 10^6$, while $\beta_I = 10^2$ allows some interpenetration to regularize small kinks.

are calculated using a continuous, piecewise linear function space, our penalized inversion using a discontinuous, piecewise linear function space, and the domain integral method of [25]. The domain integral method, which calculates the tractions via a weighting function of stress in a region around the fault, results in a smoothed solution for tractions, which results in early arrival times for the rupture. While all approaches converge at the expected rates, the discontinuous method is the most accurate, as shown in Fig. 7. Key differences in the traction solutions are shown in Fig. 8. We note, however, that as long as the rupture front is captured accurately, the slip and slip rate are robust to variations in the calculated traction as tractions are integrated before inclusion in the displacement solution.

4.2. Static simulations on complex fault networks

To demonstrate the type of domains on which we wish to simulate, a second example problem solves the elasto-static Mode II problem with constant frictional coefficient on a more realistic domain of many faults. This domain includes 26 vertical faults in the Eastern California Shear Zone from the SCEC Community Fault Model [40] surface traces, including faults east of the southern San Andreas fault in southern California, as shown in Fig. 9. The bulk domain is discretized on a Cartesian, regular mesh with grid spacing $h = 2$ km.

Initially, all faults are considered stuck with zero slip, and the static problem is solved at a fixed loading time. This static problem consists of Eqs. (16)–(18), in which inertial terms have been ignored to consider long-time, steady-state effects. Then, stress $\boldsymbol{\sigma}$ on the faults is calculated via Section 3.3, and all fault segments satisfying (31) given a maximum constant static stress coefficient Φ_s, are set to fail. On these faults, tractions are set as $f = \text{sign}(\hat{\mathbf{t}} \cdot \boldsymbol{\sigma} \cdot \hat{\mathbf{n}})\Phi_s\sigma_n$. This solution is iterated to convergence via a simple fixed-point iteration, which proves sufficient for simple problems.

In the two-dimensional, Mode II elasticity problem, any variation from planar faults results in locking, or zero slip at the kink. This locking is an artifact of the model, due to the discrete, piecewise linear representation of faults which are actually curves. Regularizing these singularities is easily accomplished under Nitsche's method; we relax the no-interpenetration constraint by decreasing β_I, allowing small interpenetration/dilation at kinks to regularize these singularities. β_I is chosen to be 10^2 by numerical experimentation; at this value, small kinks due to geometric approximations are regularized while major features of the geometry are respected.

Solutions for slip on faults and stress in the bulk are summarized in Fig. 10 for two problems, one with $\Phi_s = 0$ and one with $\Phi_s = 0.7$, one estimate for average friction on faults. This example serves to demonstrate that, even in relatively small simulations, a large number of geometrically complex faults can be represented in the simulation.

5. Conclusions

Current research indicates that fault geometry plays an important role in the physics of both earthquake dynamics and static deformation. Accurate depiction of the fault system, including many, rough faults in a computational mesh has proven a difficult task for current mesh generation techniques. Generating meshes which incorporate fault surfaces while maintaining good computational properties has proven a limitation of current techniques for fault system simulation.

The XFEM provides a alternate way of including fault system geometry in computations. We demonstrate an application of the XFEM, using Nitsche's method to incorporate the mixed boundary conditions needed on fault systems for rupture. In this method, faults are included independently of the background mesh, while extra basis functions which enable discontinuities and tip singularities are added to the approximation space. Stress on those faults are calculated using an inversion process, friction is updated, and the stick/slip nature of the rupture process is accomplished weakly.

We demonstrate the method on a community verification benchmark, and see good agreement with established solutions when faults are on element edges and when coordinate systems are rotated so that faults are no longer on element edges. We compare several methods for inverting a solution on the entire domain for tractions on the fault to update friction and failure, and find that, as long as the rupture front is accurately captured, slip and slip rate calculations are robust to the choice of method. Finally, the method is demonstrated on a fault system with many, nonplanar faults. This method demonstrates much potential for short-term crustal deformation simulations on complex fault networks, and is being actively used in scientific research, as we begin to consider the role of fault system geometry in short-term crustal deformation simulations.

Acknowledgements

ETC was supported by the Department of Energy Computational Science Graduate Fellowship Program of the Office of Science and National Nuclear Security Administration in the Department of Energy under contract DE-FG02-97ER25308. All authors were also supported by the National Science Foundation Collaboration in Mathematical Geosciences Grant EAR-0934736. BES was additionally supported by NSF Grant EAR-0911221. The authors would also like to thank three anonymous reviewers, all of whom provided helpful advice.

Appendix A. Nitche's method

Nitsche's method enables essential boundary conditions to be implemented within the weak formulation, relaxing constraints on the function spaces admitted. This has several advantages to standard Dirichlet-projection methods. Most notably, Nitsche's method in extended finite element methods is identical to that on a standard method, whereas standard techniques are difficult if not impossible to use for XFEM. Here we present the method, deriving first a bilinear form for a general problem, and then note changes needed to arrive at (19) and (20).

We start by considering a more typical elasticity problem, of

$$\nabla \cdot \boldsymbol{\sigma}(\mathbf{u}) = 0 \tag{A.1}$$

with constitutive relations as in (3) and (4) and boundary conditions given by:

$$\mathbf{u}|_{\Gamma^D} = \mathbf{g}, \tag{A.2}$$

$$\boldsymbol{\sigma}(\mathbf{u}) \cdot \hat{\mathbf{n}}|_{\Gamma^N} = \mathbf{f}. \tag{A.3}$$

The strong form is multiplied by test functions $\mathbf{v}$ from an appropriate space $\mathcal{V}$ and integrated over the domain. Green's Identity is applied, resulting in the usual variational form with natural boundary conditions included:

$$\forall \mathbf{v} \in \mathcal{V}, \int_\Omega \boldsymbol{\epsilon}(\mathbf{v}) : \boldsymbol{\sigma}(\mathbf{u}) = \int_\Gamma \mathbf{v} \cdot \boldsymbol{\sigma}(\mathbf{u}) \cdot \hat{\mathbf{n}} = \int_{\Gamma^N} \mathbf{v} \cdot \mathbf{f} + \int_{\Gamma^D} \mathbf{v} \cdot \boldsymbol{\sigma}(\mathbf{u}) \cdot \hat{\mathbf{n}}. \tag{A.4}$$

In the typical variational formulation, $\mathcal{V} = \mathcal{V}_0$ is taken to be a subset of $\mathcal{H}_0^1$, functions whose derivatives are square integrable and, crucially, have the additional constraint that $\mathbf{v}|_{\Gamma^D} = 0$. In this approach,

the last term in (A.4) vanishes. Under the Galerkin method, $\mathbf{v} \in \mathcal{V}_0^h \subset \mathcal{V}_0$, and $\mathbf{u} = \sum_i u_i \phi_i + \mathbf{u}^{\Gamma^D}$, where the $\mathbf{u}^{\Gamma^D}$ is taken to match g on Γ^D, either weakly or at node points. Construction of such a boundary solution is not well-posed in the XFEM.

Therefore we turn to Nitsche's method. The standard variational form (A.4) is equivalent to the minimization of a functional, where we look to find an approximate solution $\tilde{\mathbf{u}}$:

$$\tilde{\mathbf{u}} \equiv \arg\min_{\mathbf{v}\in\mathcal{V}_0} \mathcal{J}^*[\mathbf{v}-\mathbf{u}], \tag{A.5}$$

where

$$\mathcal{J}^*[\mathbf{w}] \equiv \int_\Omega \boldsymbol{\epsilon}(\mathbf{w}) : \boldsymbol{\sigma}(\mathbf{w}). \tag{A.6}$$

This is also known as the strain-energy formulation, where the error in the solution must minimize the strain-energy functional. To relax the requirement that this functional be minimized over a function space which vanishes on the Dirichlet boundary, Nitsche introduces additional terms, instead minimizing a new functional. The minimization formulation is no longer over $\mathcal{V}_0$, but all of $\mathcal{V}$, and the solution is given by:

$$\text{find } \tilde{\mathbf{u}} \equiv \arg\min_{\mathbf{v}\in\mathcal{V}} \mathcal{J}[\mathbf{v}-\mathbf{u}], \tag{A.7}$$

where

$$\mathcal{J}[\mathbf{w}] \equiv \int_\Omega \boldsymbol{\epsilon}(\mathbf{w}) : \boldsymbol{\sigma}(\mathbf{w}) - \int_{\Gamma^D} \mathbf{w}\cdot\boldsymbol{\sigma}(\mathbf{w})\cdot\hat{\mathbf{n}} + \beta\int_{\Gamma^D}\mathbf{w}\cdot\mathbf{w}. \tag{A.8}$$

If $\mathcal{J}$ achieves its minimum at $\mathbf{u}^h - \mathbf{u}$,

$$\frac{\partial}{\partial\delta}\mathcal{J}[\mathbf{u}-\mathbf{u}^h+\delta\mathbf{v}]|_{\delta=0} = 0 \tag{A.9}$$

for variations of length δ in all possible search directions $\mathbf{v} \in \mathcal{V}$. Differentiating, evaluating at $\delta = 0$, and substituting boundary conditions and operators for $\mathbf{u}$ from (4) and (A.3) results in the variational formulation:

$$\mathcal{B}(\mathbf{u}^h, \mathbf{v}) = \ell(\mathbf{v}) \quad \forall \quad \mathbf{v} \in \mathcal{V}, \tag{A.10}$$

where

$$\mathcal{B}(\mathbf{u},\mathbf{v}) = \int_\Omega \boldsymbol{\epsilon}(\mathbf{v}) : \boldsymbol{\sigma}(\mathbf{u}) - \int_{\Gamma^D}\mathbf{v}\cdot\boldsymbol{\sigma}(\mathbf{u})\cdot\hat{\mathbf{n}} + \boldsymbol{\sigma}(\mathbf{v})\cdot\hat{\mathbf{n}}\cdot\mathbf{u} + \frac{\beta}{h}\int_{\Gamma^D}\mathbf{v}\cdot\mathbf{u} + (\mathbf{v}\cdot\hat{\mathbf{n}})(\mathbf{u}\cdot\hat{\mathbf{n}}), \tag{A.11}$$

$$\ell(\mathbf{v}) = \int_{\Gamma^N}\mathbf{v}\cdot\mathbf{f} - \int_{\partial\Omega}\boldsymbol{\sigma}(\mathbf{v})\cdot\hat{\mathbf{n}}\cdot\mathbf{g} + \frac{\beta_{\partial\Omega}}{h}\int_{\partial\Omega}\mathbf{v}\cdot\mathbf{g} + (\mathbf{v}\cdot\hat{\mathbf{n}})(\mathbf{g}\cdot\hat{\mathbf{n}}). \tag{A.12}$$

This formulation is clearly consistent with (A.4) as when $\mathbf{u}^h = \mathbf{g}$ on the boundary and $\mathbf{v}|_{\Gamma^D} = 0$, all terms but those in (A.4) cancel. Hansbo and collaborators [22,24,6] have demonstrated coercivity of (A.11) and therefore optimal convergence rates given large enough penalty parameters.

To adjust this variational form for rupture simulation as specified in Section 2, appropriate penalty terms for the various components of the interfacial conditions are introduced. The resulting minimization formulation corresponding to Eqs. (4)–(10) is given by:

$$\begin{aligned}\mathcal{J}[\mathbf{w}] \equiv{}& \int_\Omega \boldsymbol{\epsilon}(\mathbf{w}) : \boldsymbol{\sigma}(\mathbf{w}) - \int_\Gamma (\llbracket\mathbf{w}\rrbracket_\Gamma\cdot\hat{\mathbf{n}})\sigma_n(\mathbf{w}) + \frac{\beta_I}{h}\int_\Gamma |\llbracket\mathbf{w}\rrbracket_\Gamma\cdot\hat{\mathbf{n}}|^2 \\ &- \int_{\Gamma^D}(\llbracket\mathbf{w}\rrbracket_{\Gamma^D}\cdot\hat{\mathbf{t}})\tau(\mathbf{w}) + \frac{\beta_D}{h}\int_{\Gamma^D}|\llbracket\mathbf{w}\rrbracket_{\Gamma^D}\cdot\hat{\mathbf{t}}|^2 - \int_{\partial\Omega}\mathbf{w}\cdot\boldsymbol{\sigma}(\mathbf{w})\cdot\hat{\mathbf{n}} \\ &+ \frac{\beta_{\partial\Omega}}{h}\int_{\partial\Omega}|\mathbf{w}|^2 + |\mathbf{w}\cdot\hat{\mathbf{n}}|^2\end{aligned} \tag{A.13}$$

and

$$\begin{aligned}\mathcal{J}[\mathbf{w}] \equiv{}& \int_\Omega \rho\mathbf{w}\cdot\frac{\partial^2\mathbf{w}}{\partial t^2} + \int_\Omega \boldsymbol{\epsilon}(\mathbf{w}) : \boldsymbol{\sigma}(\mathbf{w}) - \int_\Gamma (\llbracket\mathbf{w}\rrbracket_\Gamma\cdot\hat{\mathbf{n}})\sigma_n(\mathbf{w}) \\ &+ \frac{\beta_I}{h}\int_\Gamma |\llbracket\mathbf{w}\rrbracket_\Gamma\cdot\hat{\mathbf{n}}|^2 - \int_{\Gamma^D}(\llbracket\mathbf{w}\rrbracket_{\Gamma^D}\cdot\hat{\mathbf{t}})\tau(\mathbf{w}) \\ &+ \frac{\beta_D}{h}\int_{\Gamma^D}(\llbracket\mathbf{w}\rrbracket_{\Gamma^D}\cdot\hat{\mathbf{t}}|)|\left(\llbracket\frac{\partial\mathbf{w}}{\partial t}\rrbracket_{\Gamma^D}\cdot\hat{\mathbf{t}}\right) - \int_{\partial\Omega}\mathbf{w}\cdot\boldsymbol{\sigma}(\mathbf{w})\cdot\hat{\mathbf{n}} \\ &+ \frac{\beta_{\partial\Omega}}{h}\int_{\partial\Omega}|\mathbf{w}|^2 + |\mathbf{w}\cdot\hat{\mathbf{n}}|^2\end{aligned} \tag{A.14}$$

for the quasistatic and dynamic problems, respectively. Applying (A.9) to these bilinear forms result in Eqs. (16)–(20).

References

[1] B.T. Aagaard, T.H. Heaton, J.F. Hall, Dynamic earthquake ruptures in the presence of lithostatic normal stresses: implications for friction models and heat production, Bull. Seismol. Soc. Am. 91 (6) (2001) 1765–1796.

[2] D.J. Andrews, Test of two methods for faulting in finite-difference calculations, Bull. Seismol. Soc. Am. 89 (1999) 931.

[3] H. Aochi, E. Fukuyama, Three dimensional nonplanar simulation of the 1992 Landers earthquake, J. Geophys. Res. 107 (2002).

[4] I. Babuska, Finite-element method with Lagrangian multipliers, Numer. Math. 20 (3) (1973) 179–192.

[5] I. Babuska, Finite-element method with penalty, Math. Comput. 27 (122) (1973) 221–228.

[6] R. Becker, E. Burman, P. Hansbo, A Nitsche extended finite element method for incompressible elasticity with discontinuous modulus of elasticity, Comput. Methods Appl. Mech. Engrg. 198 (41–44) (2009) 3352–3360.

[7] T. Belytschko, T. Black, Elastic crack growth in finite elements with minimal remeshing, Int. J. Numer. Methods Engrg. 45 (5) (1999) 601–620.

[8] H.S. Bhat, M. Olives, R. Dmowska, J.R. Rice, Role of fault branches in earthquake rupture dynamics, J. Geophys. Res. Solid Earth 112 (B11) (2007), doi:10.1029/2007JB005027. ISSN 0148-0227.

[9] M. Bouchon, D. Streiff, Propagation of a shear crack on a nonplanar fault: a method of calculation, Bull. Seismol. Soc. Am. 87 (1997) 61.

[10] F. Brezzi, On the existence, uniqueness, and approximation of saddle-point problems arising from Lagrange multipliers, Rev. Fr. Autom. Inf. Rech. Oper. 8 (1974) 129–151.

[11] L A Dalguer, S M Day, Staggered-grid split-node method for spontaneous rupture simulation, J. Geophys. Res. 112 (2007) B02302.

[12] J.E. Dolbow, I. Harari, An efficient finite element method for embedded interface problems, Int. J. Numer. Methods Engrg. 78 (2) (2009). 229-25.

[13] J.E. Dolbow, N. Moes, T. Belytschko, Discontinuous enrichment in finite elements with a partition of unity method, Finite Elem. Anal. Des. 36 (3–4) (2000) 235–260.

[14] B. Duan, D.D. Oglesby, Nonuniform prestress from prior earthquakes and the effect on dynamics of branched fault systems, J. Geophys. Res. 112 (2007) B05308, doi:10.1029/2006JB004443.

[15] C.A. Duarte, J.T. Oden, An h-p adaptive method using clouds, Comput. Methods Appl. Mech. Engrg. 139 (1–4) (1996) 237–262.

[16] R. Duddu, S. Bordas, D. Chopp, B. Moran, A combined extended finite element and level set method for biofilm growth, Int. J. Numer. Methods Engrg. 74 (5) (2008) 848–870, doi:10.1002/nme.2200. ISSN 0029-5981.

[17] M. Duflot, The extended finite element method in thermoelastic fracture mechanics, Int. J. Numer. Methods Engrg. 74 (5) (2008) 827–847, doi:10.1002/nme.2197. ISSN 0029-5981.

[18] T. Elguedj, A. Gravouil, H. Maigre, An explicit dynamics extended finite element method. Part 1: Mass lumping for arbitrary enrichment functions, Comput. Methods Appl. Mech. Engrg. 198 (30–32) (2009) 2297–2317. ISSN 0045-7825.

[19] M. Ferronato, G. Gambolati, C. Janna, P. Teatini, Numerical modelling of regional faults in land subsidence prediction above gas/oil reservoirs, Int. J. Numer. Anal. Methods Geomech. 32 (6) (2008) 633–657. ISSN 0363-9061.

[20] T.P. Fries, A corrected XFEM approximation without problems in blending elements, Int. J. Numer. Methods Engrg. 75 (5) (2008) 503–532.

[21] A. Hansbo, P. Hansbo, An unfitted finite element method, based on Nitsche's method, for elliptic interface problems, Comput. Methods Appl. Mech. Engrg. 191 (47–48) (2002) 5537–5552.

[22] A. Hansbo, P. Hansbo, A finite element method for the simulation of strong and weak discontinuities in solid mechanics, Comput. Methods Appl. Mech. Engrg. 193 (33–35) (2004) 3523–3540, doi:10.1016/j.cma.2003.12.04. ISSN 0045-7825.

[23] R.A. Harris, M. Barall, R. Archuleta, B. Aagaard, J.-P. Ampuero, H. Bhat, V. Cruz-Atienza, L. Dalguer, P. Dawson, S. Day, B. Duan, E. Dunham, G. Ely, Y. Kaneko, Y. Kase, N. Lapusta, Y. Liu, S. Ma, D. Oglesby, K. Olsen, A. Pitarka, S. Song, E. Templeton, The SCEC/USGS dynamic earthquake rupture code verification exercise, Seismol. Res. Lett. 80 (1) (2009) 119–126.

[24] P. Heintz, P. Hansbo, Stabilized Lagrange multiplier methods for bilateral elastic contact with friction, Comput. Methods Appl. Mech. Engrg. 195 (33–36) (2006) 4323–4333.

[25] H. Ji, J.E. Dolbow, On strategies for enforcing interfacial constraints and evaluating jump conditions with the extended finite element method, Int. J. Numer. Methods Engrg. 61 (14) (2004) 2508–2535.
[26] N. Kame, T. Yamashita, Simulation of the spontaneous growth of a dynamic crack without constraints on the crack tip path, Geophys. J. Int. 139 (1999) 345.
[27] M.G. Koller, M. Bonnet, R. Madariaga, Modeling of dynamical crack propagation using time-domain boundary integral equations, Wave Motion 16 (1992) 339.
[28] F.S. Liu, R.I. Borja, Stabilized low-order finite elements for frictional contact with the extended finite element method, Comput. Methods Appl. Mech. Engrg. 199 (37–40) (2010) 2456–2471. ISSN 0045-7825.
[29] M.A. Liu, H. Wang, Q.S. Li, Inception of the Eastern California shear zone and evolution of the Pacific-North American plate boundary: from kinematics to geodynamics, J. Geophys. Res. Solid Earth 115 (B07401) (2010) 12.
[30] S.T. Marshall, M.L. Cooke, S.E. Owen, Effects of nonplanar fault topology and mechanical interaction on fault-slip distributions in the Ventura Basin, California, Bull. Seismol. Soc. Am. 98 (3) (2008) 1113–1127, doi:10.1785/0120070159. ISSN 0037-1106.
[31] J.M. Melenk, I. Babuska, The partition of unity finite element method: basic theory and applications, Comput. Methods Appl. Mech. Engrg. 139 (1–4) (1996) 289–314.
[32] N. Moes, E. Bechet, M. Tourbier, Imposing Dirichlet boundary conditions in the extended finite element method, Int. J. Numer. Methods Engrg. 67 (12) (2006) 1641–1669.
[33] N. Moes, J.E. Dolbow, T. Belytschko, A finite element method for crack growth without remeshing, Int. J. Numer. Methods Engrg. 46 (1) (1999) 131–150.
[34] H.M. Mourad, J.E. Dolbow, I. Harari, A bubble-stabilized finite element method for Dirichlet constraints on embedded interfaces, Int. J. Numer. Methods Engrg. 69 (4) (2007) 772–793.
[35] J. Nitsche, Uber ein variationsprinzip zur losung von Dirichlet-problemen bei verwendung von teilraumen, die keinen randbedingungen unterworfen sind, Abh. Math. Sem. Univ. Hamburg 36 (1970) 9–15.
[36] C.H. Scholz, The Mechanics of Earthquakes and Faulting, Cambridge University Press, 1990.
[37] B.E. Shaw, Self-organizing fault systems and self-organizing elastodynamic events on them: geometry and the distribution of sizes of events, Geophys. Res. Lett. 31 (17) (2004).
[38] B.E. Shaw, J.H. Dieterich, Probabilities for jumping fault segment stepovers, Geophys. Res. Lett. 34 (1) (2007).
[39] B.E. Shaw, J.R. Rice, Existence of continuum complexity in the elastodynamics of repeated fault ruptures, J. Geophys Res. Solid Earth 105 (B10) (2000) 23791–23810.
[40] J. Shaw, A. Plesch, G. Planansky, Community Fault Model, 2004, last updated 1/4/04.
[41] N. Sukumar, N. Moes, B. Moran, T. Belytschko, Extended finite element method for three-dimensional crack modelling, Int. J. Numer. Methods Engrg. 48 (11) (2000) 1549–1570. ISSN 0029-5981.
[42] T. Tada, E. Fukuyama, R. Madariaga, Non-hypersingular boundary integral equations for 3d non-planar crack dynamics, Comput. Mech. 25 (2000) 613.
[43] UCERF2. Working Group on California Earthquake Probabilities: The Uniform California Earthquake Rupture Forecast, Version 2. Technical report, US Geological Survey Open-File Report 2007-1437 and California Geological Survey Special Report 203, 2008.
[44] G.J. Wagner, N. Moes, W.K. Liu, T. Belytschko, The extended finite element method for rigid particles in Stokes flow, Int. J. Numer. Methods Engrg. 51 (3) (2001) 293–313.
[45] P. Wriggers, G. Zavarise, A formulation for frictionless contact problems using a weak form introduced by Nitsche, Comput. Mech. 41 (3) (2008) 407–420. ISSN 0178-7675.